



Theoretical and experimental study of gradient-helicoid metamaterial

Shanjun Liang, Tuo Liu, Fei Chen, Jie Zhu^{*}

Department of Mechanical Engineering, The Hong Kong Polytechnic University, Hung Hom, Kowloon, Hong Kong, China

ARTICLE INFO

Article history:

Received 28 July 2018

Accepted 17 October 2018

Available online 19 October 2018

Handling Editor: Erasmo Carrera

Keywords:

Acoustic metamaterial

Helical structure

Gradient index

Extraordinary transmission

Meta-lens

Focusing

ABSTRACT

Resonance based acoustic metamaterials and metasurfaces exhibit outstanding phase modulation capabilities with high transmission coefficient, but it is rather confined to the neighborhood of fundamental or harmonic resonant frequencies. Based on the impedance-matched gradient material, we theoretically and experimentally study a gradient index helicoid metamaterial that can modulate sound wavefront with nearly perfect transmission over a broad bandwidth. Taking advantage of the linear spectral phase shifting, a thin flat metalens is constructed to demonstrate sound focusing with the extraordinary transmission for more than 1/3 octave band. It is anticipated that this engineered material may be used in ultrasonography, ultrasound surgery, and DNA fragmentation. Moreover, with the flexible adjustment of effective parameters, it can be an ideal alternative to the anisotropic inhomogeneous medium and has much better stiffness.

© 2018 Elsevier Ltd. All rights reserved.

1. Introduction

The past few years witnessed the rapid expansion of study in the field of acoustic metasurface [1–13]. It enriches the acoustic wave control methodology, offering abundant unique wavefront modulation functionalities in different applications such as sound focusing [1,2,12], ultrathin absorbers [7], Bessel beam [8], self-accelerating beam, anomalous refraction [14] or reflection [3,4,11,15], cloaking [16,17], and so forth. Among them, most are based on the generalized Snell's law [5,16], suffering from limited bandwidth. There are two reasons. First, for those approaches that utilize cavity resonance based structures [12,13,18] to generate phase delay, they only work near the resonant frequencies. Secondly, if the high index is introduced by coiling up space [2,9,14], the designed metasurfaces are always accompanied by the impedance mismatching and the Fabry–Pérot resonances incurred. The dramatical decrease of the transmission coefficient occurs near to the Fabry–Pérot resonant frequencies. To extend the working frequency range, corrugated surface [19,20] and circular-holed cube [21] were adopted. They can effectively modulate the reflected acoustic wave, but not suitable for the transmitted wave. In this context, metamaterials with varying geometrical shape [10,22–26] were introduced to improve the spectral performance, as the graded interface between metamaterial and background media can decrease the reflection with a better impedance matching behavior. For some of the design [22], the high index region is restricted by the viscous or structural loss because of the structural complexity. Also, many approaches [24,27] were in a primary stage, and more experimental investigation is needed. Notably, by ‘compressing the space’ by using helicoid surface [28], a broadband dispersion-free

^{*} Corresponding author.

E-mail address: jiezhu@polyu.edu.hk (J. Zhu).

metamaterial can be obtained, and its effective parameters can be adjusted precisely by changing the helical pitch. Former works attempted to make an impedance-matched layer by using gradient pitch distribution [27,29–31] and sound devices with diverse functionalities has been demonstrated with numerical results. However, little systematic investigation has been conducted on the overall reconstruction of the uniform helicity design, especially the theoretical analysis on subsequent benefits in the frequency response of phase delay and transmission efficiency. Also, there lacks the experimental work to evaluate the effect of viscous and thermal loss and demonstrate the broadband sound wavefront modulation with high energy transfer efficiency.

In this study, we adopt helical-structured elements whose pitch is designed to change linearly along the middle axis of the cylindrical unit cells, matching the impedance of air with small helicity density at both ends. By using the transfer matrix method, we have theoretically verified the validity of the effective media model for gradient helicoid metamaterial. We have measured the performance of the energy transmission efficiency and evaluated the dispersion and loss property of a helicoid unit cell. We have proposed a flat focal lens working in a wide frequency range and experimentally measure the sound field of such a metalens. The graded helicoid metamaterial has been thoroughly studied theoretically and experimentally. Make it possible to design metamaterials whose effective characteristics and behaviors can match a corresponding inhomogeneous media. Moreover, the acoustic behavior can be predicted by the effective parameter model, which paves the way for “inverse design” from demanded character to a corresponding metamaterial structure. The helicoid bi-anisotropic metalens enriched the flexibility of acoustic metasurface.

In section 2, we study the effective parameter of the helicoid metamaterial and calculate its performance over spectrum in theory. In section 3, we experimentally test the performance of a single element of the metamaterial both in frequency domain and time domain. Also, the loss and dispersion properties are evaluated by experiment. In section 4, to show the application of the gradient helicoid metamaterial, we design a broadband focal lens and verify its performance with simulation and experimental measurement. In the end, we present the conclusions and appendices.

2. The effective model of the helicoid element

In this section, we demonstrate the characteristics and performance of the proposed metamaterial unit cell. A theoretical model of the inhomogeneous medium has been conducted to calculate the phase and transmission spectra of the element.

2.1. The structure and its acoustic characteristics

The performance of the helicoid acoustic metamaterial with constant helical pitch decays away from the Fabry–Pérot resonance frequencies, due to the impedance mismatch at two ends of the unit cells. To investigate the behavior of the graded helicoid metamaterial over a broad bandwidth and offer new wavefront modulation capability, we propose a design with linearly pitch distribution, by which the impedance matching has been improved on the interfaces. As shown in Fig. 1(a), the unit element of the proposed helical structure has the largest pitch at two ends and the smallest pitch in the middle, symmetric about the middle point. The effective impedance of such gradient helical structured unit cells is no longer uniform along the wave propagation but instead decided by the on-site pitch value.

The analytical analysis of this helical-structured metamaterial with gradient-pitched element design can be resolved with the effective medium model. We obtain the effective refractive index, mass density and impedance corresponding to a certain pitch through the retrieving method which is based on the transmission and reflection spectrum [32]. For an element with a constant diameter and gradient pitch illustrated in Fig. 1(d), the effective parameter variations along the wave propagation direction, caused by different pitch values are calculated and plotted in Fig. 1(c), (e) and (f). It is obvious that all three parameters share the same variation trend that is against the pitch change. From the end to the middle point along the Y-axis, they all increase gradually with decreasing pitch value and a tighter arrangement of the blades.

2.2. The performance over the spectrum

For a helical duct with a constant diameter, the effective parameter can be the function of the pitch. In this case, by selecting appropriate pitch distribution, a flexible and ideal inhomogeneous media can be obtained for diverse functionalities and working conditions. Based on this, the behavior of the helical-structured metamaterial elements can be estimated by the effective parameters instead of considering the circuitous geometric space. To analytically describe the relationship between the effective parameter and the position along the Y-axis, an inversely proportional function is put into use in Tables 1 and 2 to fit the distribution of index and mass density of the cell displayed in Fig. 1(e) and (f). As a symmetric profile with respect to the middle of the unit cell, the effective materials can be divided into two layers corresponding to the increasing (layer II in Fig. 2) and decreasing (layer III in Fig. 2) trend of parameters respectively. After the above operation, the geometrical model of the graded helicoid metamaterial has been replaced by the effective medium.

Outside the metamaterial region, the one-dimensional monochromatic wave equation in the background medium (layers I and IV) is (time dependency $e^{j\omega t}$ has been eliminated [34])

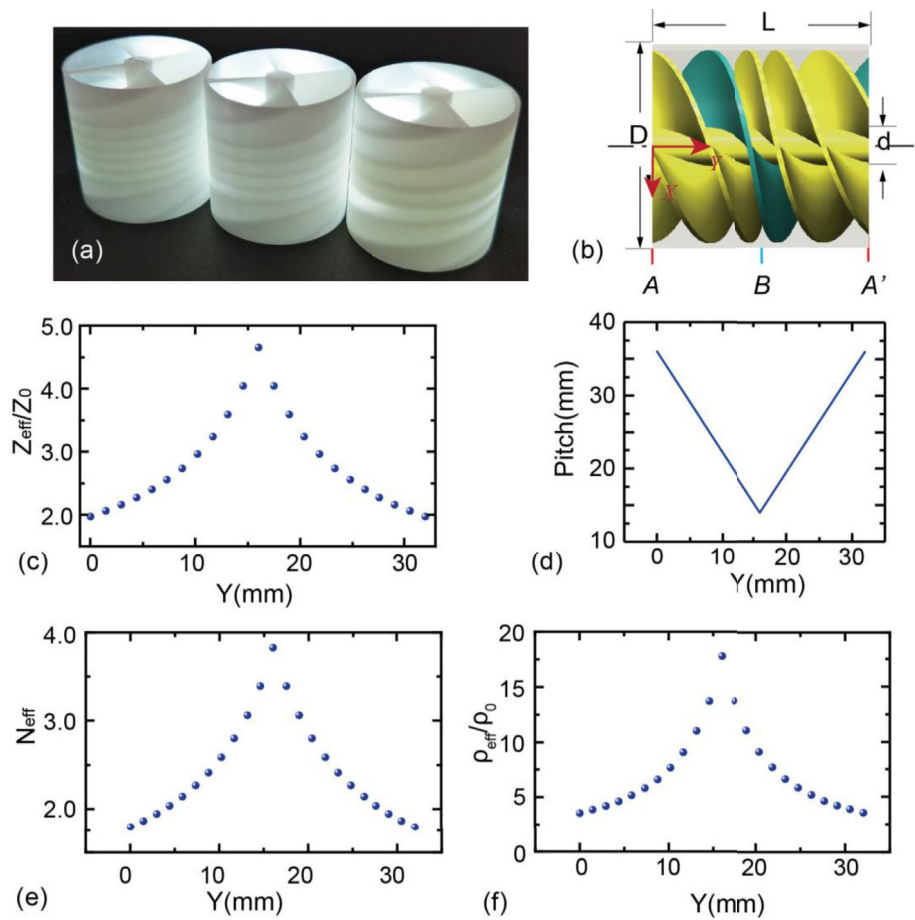


Fig. 1. The unit cell of the graded helicoid metamaterial. (a) Unit cells' photograph. (b) Detailed interior design of helical unit cell with four blades and gradient pitch. In this study, the inner diameter, outer diameter, and total length are d (6 mm), D (30 mm), and L (32 mm), respectively. (c)–(f) The distribution of effective impedance, pitch, effective refractive index and effective mass density of the gradient-pitched element.

Table 1
The fitting of the effective refractive index.

| | | | | |
|-----------------------------|--|-----------|--|------------|
| Interval of y | $0 - \frac{L}{2}$ | | $\frac{L}{2} - L$ | |
| Expression | $N_{eff} = \frac{1}{\alpha_1 y + \beta_1}$ | | $N_{eff} = \frac{1}{\alpha_2 y + \beta_2}$ | |
| Independent variable | y | | | |
| Dependent variable | N_{eff} | | | |
| Method | Trust Region method [33] | | | |
| Coefficients to be fitted | α_1 | β_1 | α_2 | β_2 |
| Result | -19.66 m^{-1} | 0.5804 | 19.66 m^{-1} | -0.04862 |
| Sum of squares due to error | 0.04375 | | 0.04375 | |

Table 2
The fitting of the effective mass density.

| | | | | |
|-----------------------------|--|--------------------------------------|--|---------------------------------------|
| Interval of y | $0 - \frac{L}{2}$ | | $\frac{L}{2} - L$ | |
| Expression | $\rho_{eff} = \frac{1}{\mu_1 y + \nu_1}$ | | $\rho_{eff} = \frac{1}{\mu_2 y + \nu_2}$ | |
| Independent variable | y | | | |
| Dependent variable | ρ_{eff} | | | |
| Method | Trust Region method | | | |
| Coefficients to be fitted | μ_1 | ν_1 | μ_2 | ν_2 |
| Result | $-10.98 \text{ kg}^{-1} \text{ m}^2$ | $0.2218 \text{ kg}^{-1} \text{ m}^3$ | $10.98 \text{ kg}^{-1} \text{ m}^2$ | $-0.1295 \text{ kg}^{-1} \text{ m}^3$ |
| Sum of squares due to error | $0.7205 \text{ kg}^2 \text{ m}^{-6}$ | | $0.7205 \text{ kg}^2 \text{ m}^{-6}$ | |

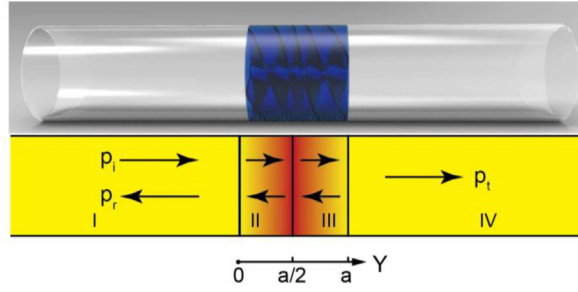


Fig. 2. The illustration of a gradient-helical-structured unit cell and background's acoustic indices.

$$\frac{d^2 p(y)}{dy^2} + \left(\frac{\omega}{c}\right)^2 p(y) = 0 \quad (1)$$

with the solution being expressed as

$$p(x) = \Psi_I^1 e^{-iky} + \Psi_I^2 e^{iky} \quad (2)$$

where Ψ_I^1 and Ψ_I^2 are constants which can be determined by the boundary conditions.

For the particle velocity along the propagation direction, we have

$$\rho \frac{\partial v}{\partial t} = -\frac{\partial p}{\partial y} \quad (3)$$

and thus

$$v_I(x) = \Psi_I^1 \frac{ke^{-iky}}{\omega \rho_0} - \Psi_I^2 \frac{ke^{iky}}{\omega \rho_0} \quad (4)$$

The wave equation of the inhomogeneous media in layers II and III has the form below [35]:

$$\frac{d^2 p_1(y)}{dy^2} + \left(\frac{\omega}{c} n_{eff}(y)\right)^2 p_1(y) - \left(\frac{d \ln \rho_{eff}(y)}{dy}\right) \frac{d}{dy} p_1(y) = 0 \quad (5)$$

where $n_{eff}(y)$ and $\rho_{eff}(y)$ are the space-dependent variables that can be expressed as

$$n_{eff} = \begin{cases} \frac{1}{\alpha_1 y + \beta_1}, & 0 \leq y \leq L/2 \\ \frac{1}{\alpha_2 y + \beta_2}, & L/2 < y \leq L \end{cases}, \quad \rho_{eff} = \begin{cases} \frac{1}{\mu_1 y + \nu_1}, & 0 \leq y \leq L/2 \\ \frac{1}{\mu_2 y + \nu_2}, & L/2 < y \leq L \end{cases} \quad (6)$$

where α_i , β_i , μ_i and ν_i ($i = 1, 2$) are the coefficients obtained by curve fitting in Tables 1 and 2

The solution of Eq. (5) has the form

$$p_{II}(x) = \Psi_{II}^1 \mathcal{A}(y) + \Psi_{II}^2 \Theta(y) \quad (7)$$

where Ψ_{II}^1 and Ψ_{II}^2 are constants for the two linearly independent solutions denoted by $\mathcal{A}(y)$ and $\Theta(y)$. The details of the solution are presented in Appendix B. Combine Eqs. (3) and (7), the particle velocity in layer II is

$$v_{II}(y) = \Psi_{II}^1 \frac{j}{\omega \rho} \frac{d\mathcal{A}(y)}{dy} + \Psi_{II}^2 \frac{j}{\omega \rho} \frac{d\Theta(y)}{dy} \quad (8)$$

In layer III the sound pressure and particle velocity have the same form as that in layer II but the values of α , β , ν and μ are different. The independent solution can be denoted by $\mathcal{A}'(y)$ and $\Theta'(y)$. With the continuity of sound pressure and normal particle velocity at the interfaces, we can obtain the following relationship for the background and effective medium layers.

$$\begin{cases} p_I(0) = p_{II}(0) \\ v_I(0) = v_{II}(0) \end{cases}, \begin{cases} p_{II}\left(\frac{a}{2}\right) = p_{III}\left(\frac{a}{2}\right) \\ v_{II}\left(\frac{a}{2}\right) = v_{III}\left(\frac{a}{2}\right) \end{cases}, \begin{cases} p_{III}(a) = p_{IV}(a) \\ v_{III}(a) = v_{IV}(a) \end{cases} \quad (9)$$

By changing Eq. (9) to matrix form and eliminating the middle term, the relationship between layer I and layer IV can be described by a matrix

$$\mathbf{T} = \mathbf{T}_{II}|_{y=a} \cdot \mathbf{T}_{II}|_{y=\frac{a}{2}}^{-1} \cdot \mathbf{T}_I|_{y=\frac{a}{2}} \cdot \mathbf{T}_I|_{y=0}^{-1} \cdot \mathbf{M}|_{y=0} \quad (10)$$

In Eq. (10),

$$\mathbf{T}_I = \begin{pmatrix} A(y) & \Theta(y) \\ \frac{j}{\omega\rho(y)} \frac{dA(y)}{dy} & \frac{j}{\omega\rho(y)} \frac{d\Theta(y)}{dy} \end{pmatrix}, \mathbf{T}_{II} = \begin{pmatrix} A'(y) & \Theta'(y) \\ \frac{j}{\omega\rho(y)} \frac{dA'(y)}{dy} & \frac{j}{\omega\rho(y)} \frac{d\Theta'(y)}{dy} \end{pmatrix},$$

$$\mathbf{M} = \begin{pmatrix} e^{-jky} & e^{jky} \\ \frac{ke^{-jky}}{\omega\rho_0} & \frac{ke^{jky}}{\omega\rho_0} \end{pmatrix}.$$

Based on the continuity of sound pressure and normal particle velocity, the relationship between the pressure p_i of incidence and transmission p_t follows the equation

$$\mathbf{T} \begin{bmatrix} p_i \\ p_r \end{bmatrix} = p_t e^{-jkl} \begin{bmatrix} 1 \\ k \\ \omega\rho_0 \end{bmatrix}, \quad \mathbf{T}^{-1} = \begin{bmatrix} t_{inv11} & t_{inv12} \\ t_{inv21} & t_{inv22} \end{bmatrix} \quad (11)$$

In Eq. (11), k and ω are the wave number and angular frequency of the plane wave; ρ_0 is the mass density of air. In this case, the overall complex transmission coefficient of sound pressure t_p is derived as

$$t_p = \frac{e^{jkl}}{t_{inv11} + \frac{k}{\rho_0} \frac{1}{t_{inv12}}}. \quad (12)$$

One needs to take into consideration is the small difference between the real structure and the effective model. Because of the large pitch of helicity at both ends of cells, the effective model can be slightly shorter than the length of the blade region (32 mm). Thus, for the numerical calculation and simulation model with an effective parameter, we cut 2 mm at both ends for more accurate results.

The calculated sound pressure transmission and phase delay through the gradient index unit cell is shown in Fig. (3). The curve in Fig. 3(a) clearly shows the transmission coefficient higher than 80% over the most frequency range. At the same time, the phase delay shows smooth variation with a gentle slope over the studied frequency range. It is because the gradient index along the propagation direction weakens the strong dispersion of phase shift caused by specific Fabry-Pérot resonance. With

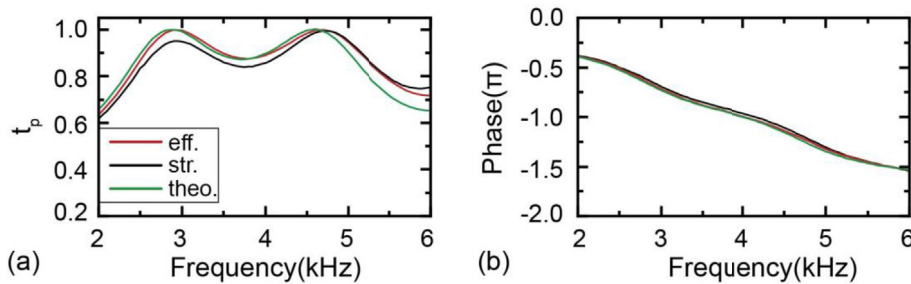


Fig. 3. The calculated performance of an element. (a) The transmission spectrum of normal incident plane waves crosses the unit cell. (b) The corresponding phase spectrum response. (a) and (b) share the same legend in (a). Note of legend: eff.—simulation results by using effective media, str.—simulation by using the helicoid model, theo.—numerical results corresponding to the theoretical analysis.

such a smooth curve, controlling the phase delay for phase engineering within the whole wide frequency range of interests is easier and more practical.

The good agreement of three groups of results in Fig. (3) indicates the feasibility of the effective medium model and the theoretical analysis. The small difference of transmission coefficient of sound pressure may come from the round-off error of the numerical computation and thickness of the structure's blades. As we can see in the illustration of the phase delay (Fig. 3(b)), a slight shift can be neglected. On the one hand, the result shows the validity of the inhomogeneous medium model to replace the real structure. Thus, the designed metamaterial with air-like acoustic properties has relatively high stiffness, which can be used as inhomogeneous sound media. On the other hand, the conformity guarantees the 'inverse design' from required material parameters' distribution to the related helical structure. This property remains a huge potential for the flexible design of acoustic metamaterial. The computation above are all in a lossless condition and the influence of viscous and thermal loss has been evaluated by experiment in the following section.

3. Experimental investigation of the helicoid element

In this section, the experiment results are illustrated to show the performance and characteristics of the graded helicoid metamaterial.

3.1. Experimentally tested performance

The performance of the newly designed helical-structured acoustic metamaterial unit cell with gradient pitch has been experimentally measured inside an impedance tube using the 4-microphone 2-load method, as shown in Fig. 4(a). The samples were manufactured by 3D printing. The huge impedance mismatch between the photopolymer (Somos GP Plus) material we used to fabricate the sample and air makes it possible for us to regard it as being rigid in theory model. We performed both time and frequency related experiments. To demonstrate that the new gradient-pitched helical-structured design still possesses the sound deceleration function, a short pulse was generated and sent inside the impedance tube. The recorded transmission signals with and without the metamaterial sample are shown in Fig. 4(b). It is evidently clear that, by adding the metamaterial unit cell, the sound signal is further delay by about 1.19×10^{-4} s. The time delay functionality for the signal transmission has been verified.

From the uniform pitch distribution to the graded model, the impedance mismatch has been weakened, so as the Fabry–Pérot resonance related to the reflection at interfaces. The difference can be observed by the comparison of transmission spectrum between elements with constant pitch and gradient pitch. Fig. 4(c) shows the experimentally measured spectral transmission performance. As anticipated, the transmission coefficient of the uniform pitched model changes violently, due to the relatively pure Fabry–Pérot resonance mode. The 3-dB half-power bandwidth is rather narrow, about 0.52 kHz.

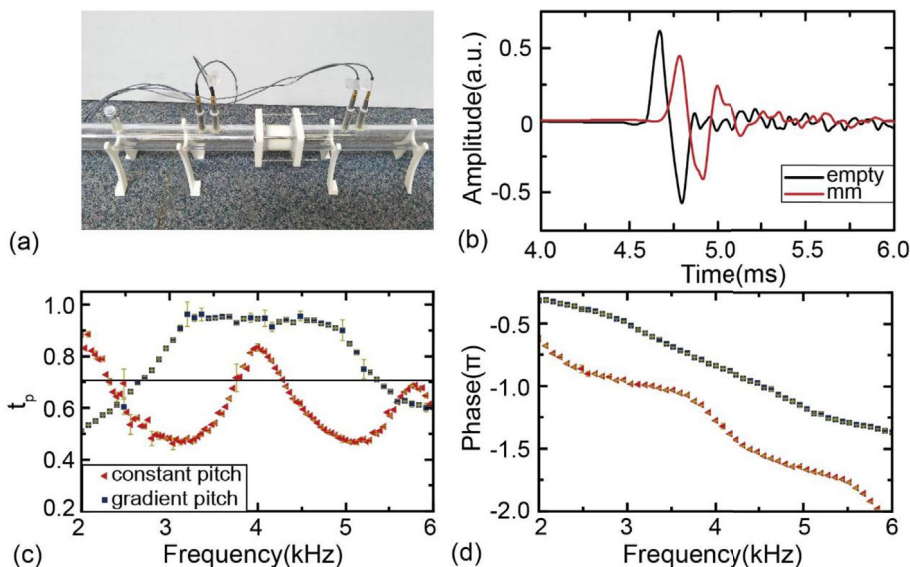


Fig. 4. Measurement of gradient helical-structured metamaterial element. (a) The setup of the lab-made impedance tube. The white-colored cell is fixed in the middle by two flanges. (b) The delay of the pulse sound signal introduced by the gradient-pitched helical-structured element. (c) The sound pressure transmission coefficient of a uniform-pitched and gradient pitched element. (d) Phase shift spectra of a uniform-pitched and gradient pitched element. For the uniform-pitched element, the leading pitch is 20 mm; for the gradient pitched unit cell, the pitch distribution is the same as Fig. 1(d). Note of legend: mm—with metamaterial layer.

Represented by the blue curve, the transmission through the gradient-pitch unit cell remains at high values close to unity over a wide frequency range, in good agreement with the prediction from the transfer matrix method. The 3 dB half-power band is now 2.6 kHz wide, covering from 2.68 kHz to 5.28 kHz, about one octave. Such extraordinary sound pressure transmission of the gradient-pitched model over spectrum can be attributed to two physical mechanisms: the better impedance matching with the background medium at two ends of the unit cell due to the large pitch there, and the gradient index profiles that can bridge more sound energy through to counter the effects of specific Fabry–Pérot resonance mode. Fig. 4(d) demonstrates the measured phase shift of the two unit cells. While the gradient-pitched unit cell shows a smooth phase delay curve without a notable inflection point in the 3-dB band, the phase shift offered by the uniform-pitched unit cell fluctuates around the resonant frequency at 4 kHz.

3.2. Evaluation of the loss and dispersion

The previous work [30] pointed out the dispersion-free property of the uniform-pitched element, while the dispersion property of the gradient-pitched model has not been experimentally studied. To sufficiently evaluate the characteristic of the helicoid metamaterial, we calculated the spectra of energy transmission and reflection. Thus, the viscous and thermal loss of the element can be obtained according to the relationship

$$TL = 1 - t_I - r_I \quad (13)$$

where TL is the energy loss, t_I and r_I are the transmission and reflection coefficients of the energy. We can see that the thermal and viscous loss keeps at a low level over the spectrum (Fig. 5(a)). As a contrast, the energy loss of a uniform-pitched element shows a larger loss near the resonance frequency. The small loss can also be further demonstrated by the effective refractive index. As the gradient distribution of the helical pitch, retrieving of effective parameters cannot be straightforward. However, we can measure the average value of the effective refractive index by taking it as a homogeneous medium. The real part of the index in Fig. 5(b) shows the dispersion-free property of the graded helical duct over the spectrum. The imaginary part – the attenuation coefficient – is near to zero and keeps flat during the calculated frequency range. Hence the gradient-pitched helical structure can be described by a lossless model reasonably.

4. A helicoid-metamaterial-based diffractive focal lens

In this section, a flat focal lens works in a wide frequency range has been realized. According to the characteristic of the lens, the position of the focal spot at the different operating frequency is calculated and verified by experiment.

4.1. Lens design

The new helical-structured acoustic metamaterial with gradient pitch offers extraordinary sound transmission and smooth phase adjustment within a wide frequency range. Therefore, it is now possible to realize a series of phase delays by appropriate pitch distributions, without the fear of suffering from the lower transmission. With the smooth phase shift, the difference of phase delay between any two unit cells keeps invariable over the spectrum. Taking advantage of this unique characteristic, we design and fabricate a thin flat focal lens with the array of new gradient-pitched helical-structured acoustic metamaterial unit cells, whose thickness is less than half of the smallest wavelength. To design a focal lens for normally incident transmitted plane wave, the geometrical relationship illustrated in Fig. 6(b) should be satisfied with the equation

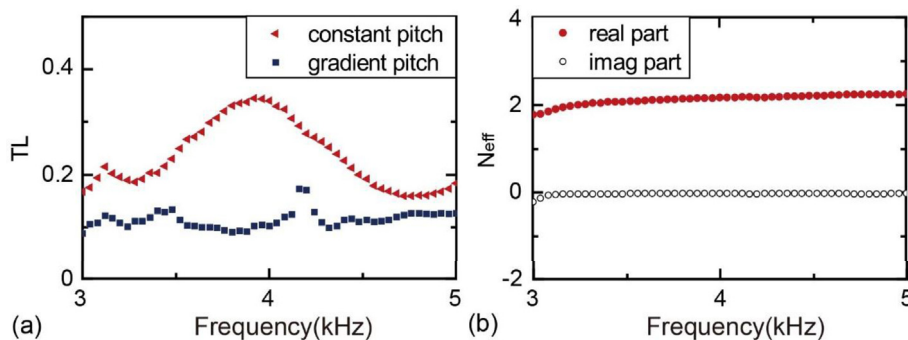


Fig. 5. The energy loss and effective index. (a) The measured viscous and thermal loss of uniform and graded helicoid cell. (b) The measured average refractive index of the graded helicoid cell.

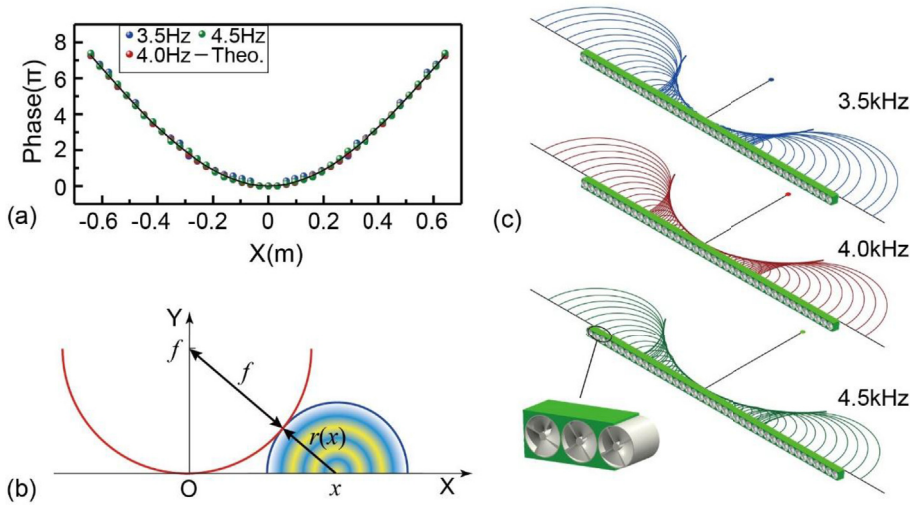


Fig. 6. Design of the focal lens with excellent sound transmission. (a) Phase profile requirement of the flat focal lens for different sound frequencies. The dots represent the phase of each unit cell at the corresponding positions, and the black line is the theoretically designed phase profile at 4 kHz by Eq. (14). (b) The geometric relationship between focal length and the wavefront of a point source at position x . The gradual change in radiation means a unit cell can be regarded as a point source. (c) The focal point for three operating frequencies. The semicircle is the wavefront from each unit cell. The envelope curve obtained by fitting method appears in bold is the focusing wavefront. At the bottom left corner of (c), the structure of the flat lens is magnified partially. Forty-one cells are embedded in the holey frame whose total width is 1.312 m.

$$\varphi(x) = \frac{2\pi f}{c} \left(\sqrt{x^2 + F^2} - F \right). \quad (14)$$

Eq. (14) gives the required phase adjustment distribution along the surface the of the flat focusing lens, where φ denotes the phase delay at any specific location x , f is the operating frequency, c is the sound speed in the air (343.2 m s^{-1}), and F is the focal length. This continuous phase profile is further discretized into 41 segments so that the whole lens can be constructed with 41 individual unit cells embedded in a holding frame, just as exhibited in Fig. 6(c). The required phase modulation at each of the forty-one unit cells is achieved by adjusting the leading pitch. We subsequently calculate the phase profiles for three different frequencies 3.5 kHz, 4 kHz and 4.5 kHz and present the discretization results in Fig. 6(a). Because of the smooth phase delay of the elements about frequency, any two elements can keep a relatively constant phase difference over the spectrum, which forms a uniform phase profile. This paves the way towards realizing broadband sound focusing with one set of gradient-pitched helical-structured acoustic metamaterial unit cells array. Since the consistency of the phase distribution about the frequency, the position of the focal point is frequency dependent and can be predicted. In Eq. (14), taking F as the parameter to be fitted, x and $\varphi(x)$ as the independent and dependent variables, we can obtain the focal length at different frequencies with curve fitting method. In the process of fitting, we firstly have an expression

$$y = \frac{c}{2\pi f} \varphi(x) = \sqrt{x^2 + F^2} - F \quad (15)$$

where y is the wavefront based on the phase profile. By using the trust region fitting method, the focal length F can be obtained. As shown in Fig. 6(c), the radius of the output wavefront envelope, i.e., the focal length, will increase with frequency, being 0.40 m at 3.5 kHz, 0.50 m at 4 kHz and 0.58 m at 4.5 kHz, respectively.

4.2. Field measurement of broadband focusing

We conducted simulation and experiments to validate the thin flat focal lens design. The sound intensity patterns for three separated frequencies 3.5 kHz, 4 kHz and 4.5 kHz are extracted and plotted in Fig. 7. Due to the limited range of our sound mapping system, we only measured the region around the focal point, marked with red boxes in Fig. 7(a)–(c) and illustrated by Fig. 7(d)–(f). From the well-matched simulation and experiment results, it is evidently clear that the thin flat lens can focus incident acoustic waves of different frequencies covering 1/3 octave coverage. The shape of the focal spot is clear for all three frequencies. The sound intensity at the focal point also remains on the same level for three frequencies, indicating similar high transmission over the spectrum. Simulations for incident acoustic waves with frequencies different from the previous three ones were also conducted. In all cases, the similar extraordinary sound transmission and focusing effects can be clearly observed. Please refer to Appendix C for the predicted behavior and the pressure field. The high energy transmission

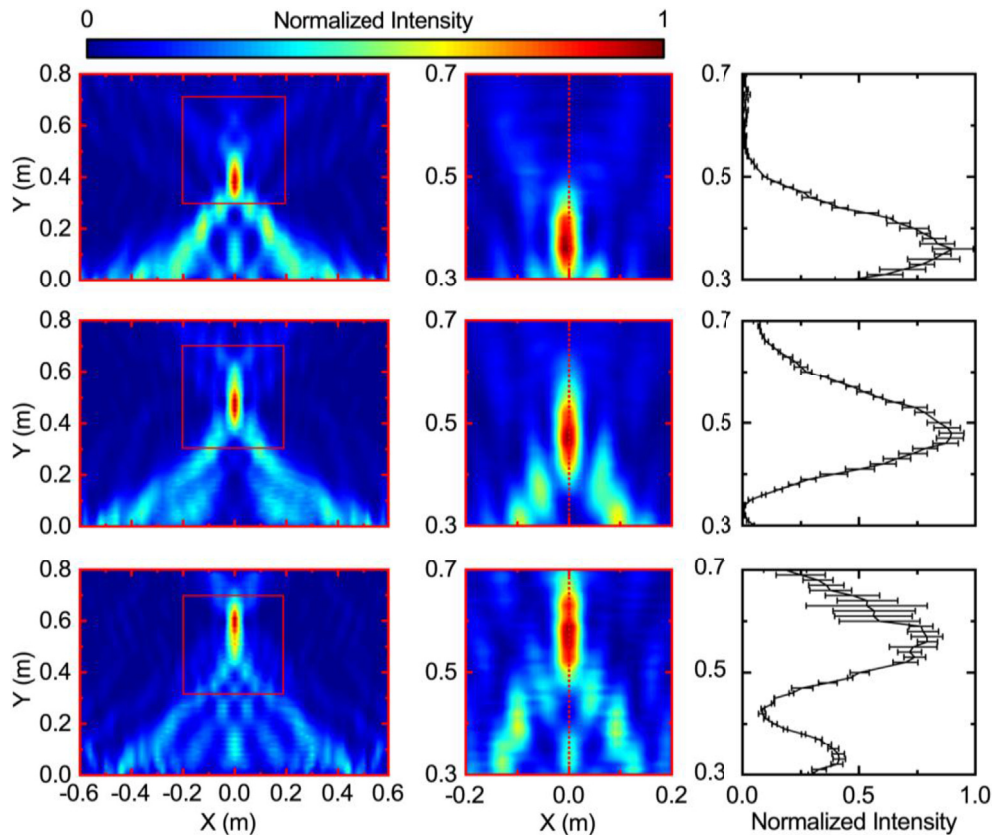


Fig. 7. The intensity field of broadband sound focusing. (a)–(c) The simulated sound intensity field distribution at 3.5 kHz, 4 kHz and 4.5 kHz, respectively. The red blocks inside mark the scanning area adopted in the experiments. (d), (e) and (f) are the experimentally measured sound intensity field distribution at 3.5 kHz, 4 kHz and 4.5 kHz, respectively. (g), (h) and (i) are the transverse cross-section intensity distribution along the Y-axis (the red dash lines) at $x = 0$ for 3.5 kHz, 4 kHz and 4.5 kHz, respectively. (For interpretation of the references to color in this figure legend, the reader is referred to the Web version of this article.)

coefficient in the whole operating frequency range is witnessed by almost the same maximum intensity under 3.5 kHz, 4 kHz and 4.5 kHz as is shown in Fig. 7(g)–(i). What is noteworthy is that in the wave travelling direction the intensity drops sharply after passing through the focal spot. This behavior is of great significance in contributing to the concentration of energy. By observing the position of the peak, the experimentally determined focal length is 0.36 m, 0.47 m, and 0.56 m for the corresponding frequency in Fig. 7(g)–(i). The small difference between the theoretical and experimental results of focal length indicates the good controllability and high accuracy of the lens. The error of the experiment may come from the slight shaking of the microphone during the test process. The intensity gradient near the focal spot is so steep that a slight shaking may lead to a large error.

5. Conclusions

In this study, we investigated the acoustic characteristic of the graded helicoid metamaterial and constructed a broadband focal lens with the studied element cell. With the gradient pitch design, the new helical-structured acoustic metamaterial provides better impedance matching with the background medium at two ends and bridges more sound energy through to counter the effects of Fabry–Pérot resonance mode. A more detailed theoretical model has been established for the evaluation of the unit cell's performance and providing the possibility of inverse design from acoustic parameter distribution to its geometric parameter counterparts.

We experimentally verified its performance and the validity of the theoretical analysis. The measured effective index shows the low viscous and thermal loss over the spectrum and the dispersion-free property of the graded helicoid metamaterial, adding substantial evidence for the practical use. We subsequently design and fabricate a thin meta-lens with the gradient-pitched helical-structured metamaterial and the frequency-dependent focal point position has been calculated. The high performance of sound focusing effect is then verified experimentally with the lens over multiple frequencies. This study provides a flexible and precise alternative for the inhomogeneous media. The helical structures have adjustable acoustic parameters and stiff body. It will not only benefit the physics research on realizing wavefront modulation with novel passive materials but also be anticipated that this new metamaterial might be used in ultrasonography, ultrasound surgery or DNA

fragmentation, which need to focalize the energy to a specific region. By using the gradient helicoid metamaterial to meet the requirement, we can make gradient index to obtain extremely high sound pressure through wave compression, which can work in a wide frequency range.

Acknowledgements

The work was supported by the Early Career Scheme (ECS) of Hong Kong RGC [grant number 25208115]; the Departmental Internal Competitive Research Grant [grant number G-UA8T] from the Hong Kong Polytechnic University.

Appendix A. The fitted results of effective parameters

Firstly, the trust region method is commonly used for curve fitting or optimization, Helfrich [33] gave a detailed description of curve fitting. Secondly, to show the excellent agreement between the fitting result and the original data, we put a chart for comparison. The excellent agreement between the fitting result and effective parameter shows the efficiency of the method.

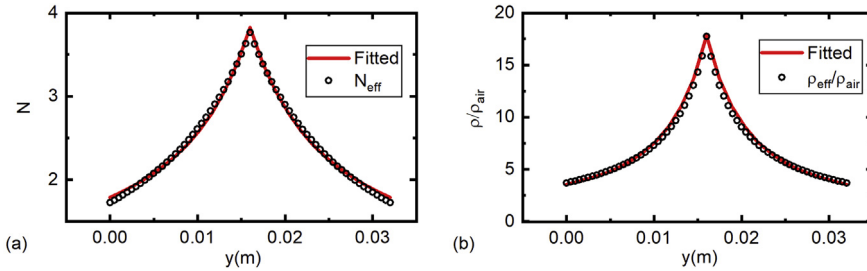


Fig. A.1. Fitting of the effective parameter (a) The comparison of the fitted index and the original data (b) The comparison of the fitted density and the original data.

Appendix B. The solution of the inhomogeneous equation

Considering the complexity of the mentioned inhomogeneous equation, we resort to the symbolic calculation of computer software. The solution of Eq. (5) can be written as

$$\begin{aligned} p_{II}(x) &= \Psi_{II}^1 F([n_1, n_2], d, z) \cdot (\alpha y + \beta)^{-\frac{1}{2} \frac{\sqrt{\alpha^2 c^2 - 4\omega^2} - c\alpha}{c\alpha}} + \\ &\Psi_{II}^2 F([n'_1, n'_2], d', z') \cdot (\alpha y + \beta)^{-\frac{1}{2} \frac{\sqrt{\alpha^2 c^2 - 4\omega^2} + c\alpha}{c\alpha}} \\ &= \Psi_{II}^1 \mathcal{A}(y) + \Psi_{II}^2 \Theta(y) \end{aligned} \quad (\text{B.1})$$

where $F([n_1, n_2], d, z)$ is the hypergeometric function which has the form

$$F([n_1, n_2], d, z) = \sum_{k=0}^{\infty} \frac{z^k \Gamma(n_1 + k) \Gamma(n_2 + k) \Gamma(d)}{k! \Gamma(n_1) \Gamma(n_2) \Gamma(d + k)}. \quad (\text{B.2})$$

Meanwhile, Ψ_{II}^1 and Ψ_{II}^2 are constants for the two linearly independent solutions denoted by $\mathcal{A}(x)$ and $\Theta(x)$. For details,

$$\begin{aligned} n_1 &= -\frac{1}{2} \frac{\sqrt{\alpha^2 c^2 - 4\omega^2} - 2j\omega - c\alpha}{c\alpha}, n_2 = -\frac{1}{2} \frac{\sqrt{\alpha^2 c^2 - 4\omega^2} + 2j\omega - c\alpha}{c\alpha} \\ d &= \frac{-\sqrt{\alpha^2 c^2 - 4\omega^2} + c\alpha}{c\alpha}, z = \frac{(\alpha y + \beta)\mu}{-\alpha v + \beta\mu} \\ n'_1 &= -\frac{1}{2} \frac{\sqrt{\alpha^2 c^2 - 4\omega^2} - 2j\omega + c\alpha}{c\alpha}, n'_2 = -\frac{1}{2} \frac{\sqrt{\alpha^2 c^2 - 4\omega^2} + 2j\omega + c\alpha}{c\alpha} \\ d' &= \frac{\sqrt{\alpha^2 c^2 - 4\omega^2} + c\alpha}{c\alpha}, z' = \frac{(\alpha y + \beta)\mu}{-\alpha v + \beta\mu}. \end{aligned}$$

Following the property of hypergeometric functions [36], as two general solutions of the inhomogeneous equation, $\mathcal{A}(y)$ and $\Theta(y)$ are linearly independent.

To ensure correctness, we put $\mathcal{A}(y)$ and $\Theta(y)$ back in to

$$D = \frac{d^2 p_1(y)}{dy^2} + \left(\frac{\omega}{c} n_{eff}(y) \right)^2 p_1(y) - \left(\frac{d \ln \rho_{eff}(y)}{dy} \right) \frac{d}{dy} p_1(y) \quad (B.3)$$

and D has been calculated being 0. Furthermore, the good agreement of the theory and simulation result shows the rationality of the derivation.

Appendix C. The Pressure and intensity field of sound focusing

To further demonstrate the capability, the pressure pattern of simulation and experiment has been plotted in Fig. C.1 For one thing, it clearly shows the bent wavefronts. For another, along with the frequency increase, the focal spot moves further which is in good agreement with the theoretical analysis.

The available frequency band of the designed focal lens ranges from about 3.5 kHz to 4.5 kHz, not limited to the three separated frequencies demonstrated in the main text. To intensively verify the flat lens' performance, simulations at other frequencies have been conducted. The simulated acoustic intensity fields in Fig. C.2 shows that the lens has an ideal and uniform performance for sound focusing over a considerable bandwidth.

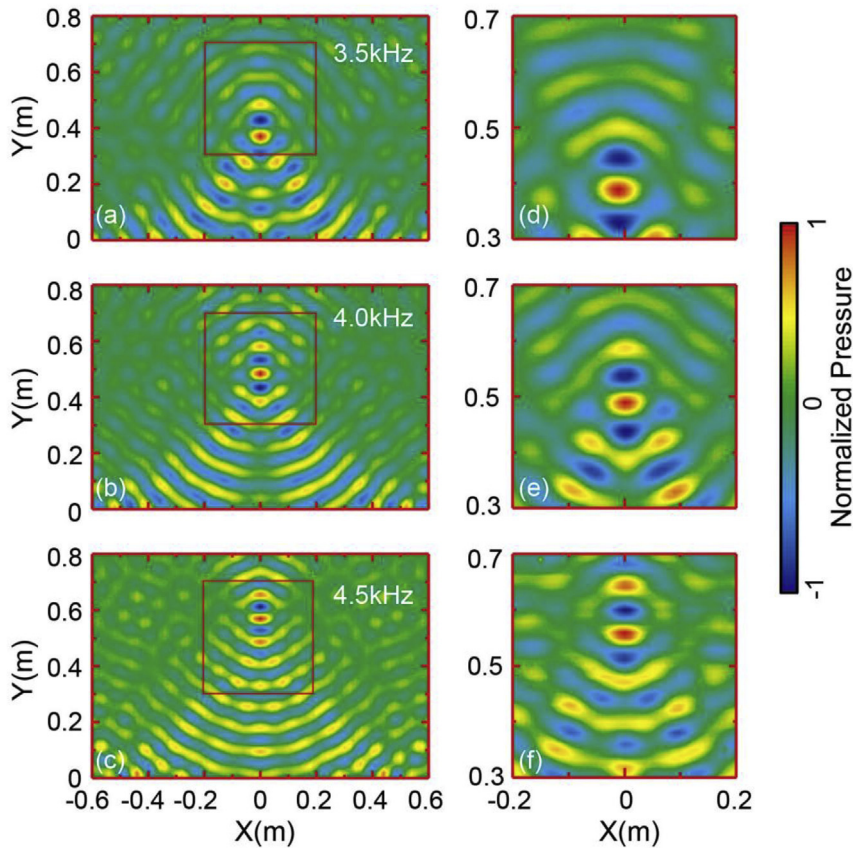


Fig. C.1. Comparison of the measured and simulated acoustic pressure fields. (a)–(c) are the simulation results and (d)–(f) are the experimental results. Red boxes in the left sub-figures denote the scanned area.

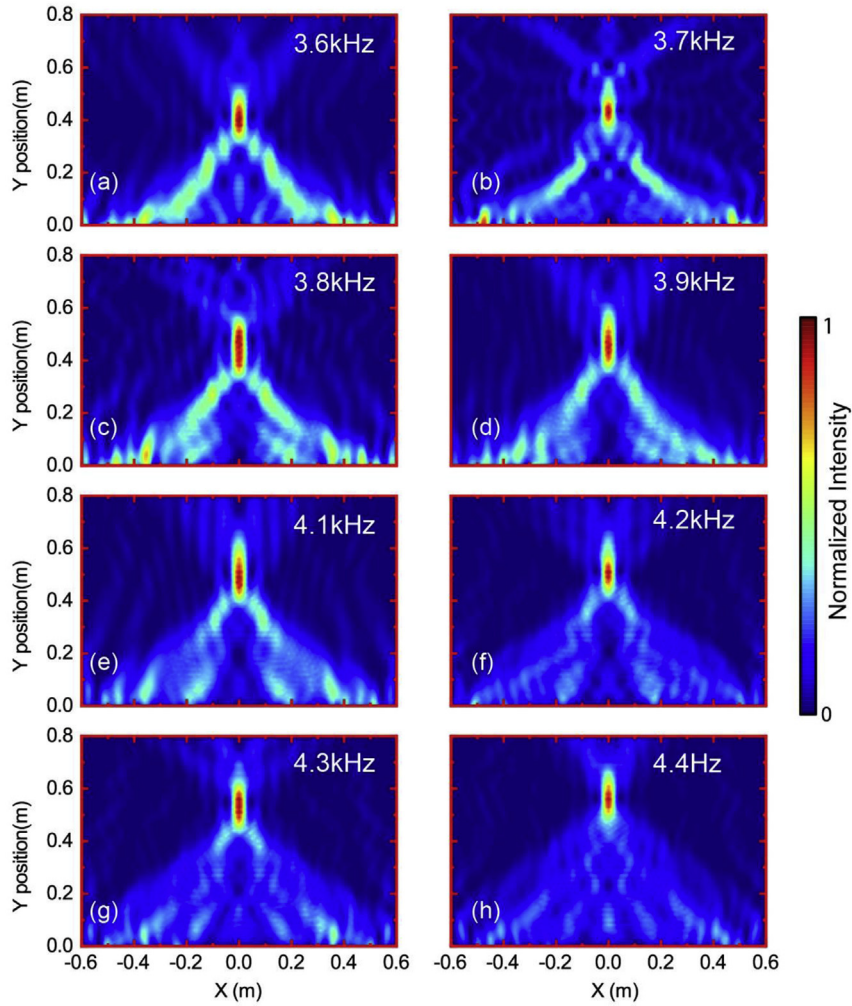


Fig. C.2. The simulated intensity distributions at several different frequencies within 3.5 kHz–4.5 kHz.

Appendix D. Full-wave simulation considering the mechanical properties of the structure

To make sure the design can work in the practical condition, we have conducted a simulation when considering the mechanical properties of the helical structure. Compared to the simulation under ideal boundary condition (rigid boundary), the good agreement of the filed patterns (Fig. D.1) indicates the rationality of the theoretical assumptions.

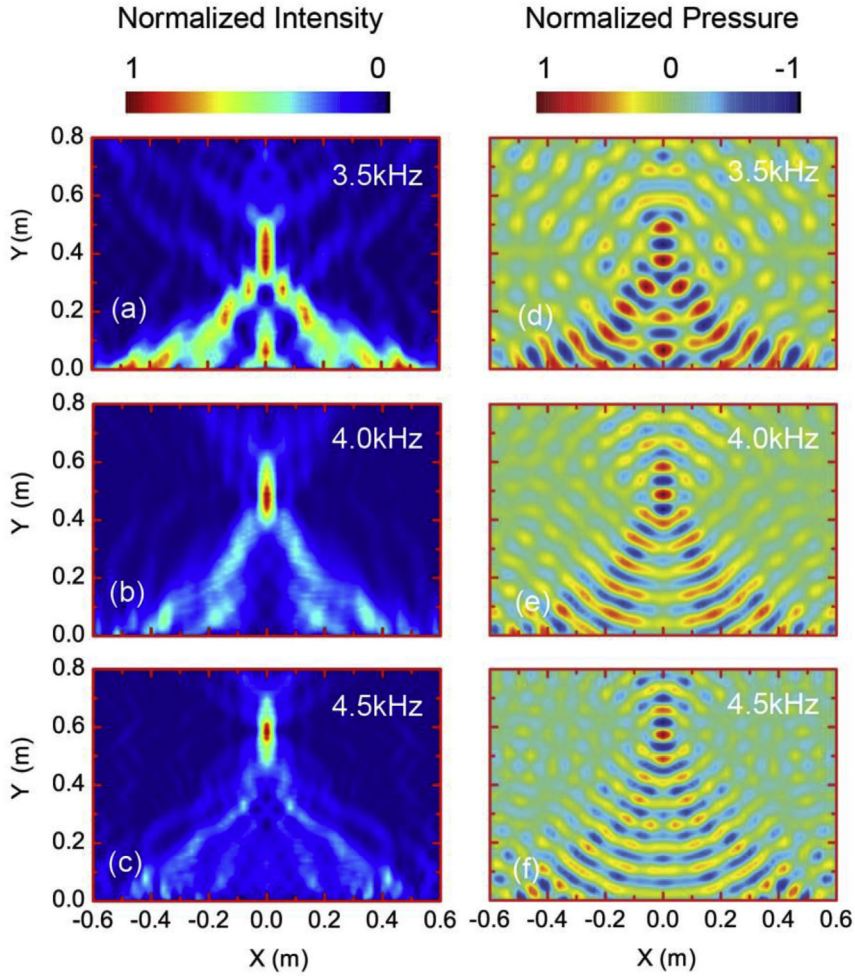


Fig. D.1. Full-wave simulation with real structure properties Fig (a)–(c) are for the intensity field and figure (d)–(f) are for the pressure field.

Appendix E. Experimental setup

The unit cells are made from photosensitive resin (material type, Somos GP Plus 14122) and printed based on laser sintering stereo-lithography. To test the complex transmission coefficient, a self-made impedance tube is used. The parts of the tube are listed as follows.

1. Source, A loudspeaker (Tymphany PMT-40N25AL01-04) driven by a signal generator (Brüel and Kjær 3560D with 7539 Controller modules and 3109 Output modules) and a power amplifier (Brüel and Kjær Type 2706)
2. The signal collection, Brüel and Kjær type microphone 1/4 inch (Type 4935)

By using the transfer matrix method and the measured complex pressure, the transmission coefficient and phase delay of the unit cell sample has been calculated.

The experiment of broadband sound focusing has been conducted in half space. To generate an experimental plane wave, thirty loudspeakers with an interval 40 mm are used to assemble a line source and synchronously driven by Zurich Instruments HF2LI Lock-in Amplifier and a power amplifier (Brüel and Kjær Type 2716C). Forty-one printed unit cells are fixed by a holey frame and the interval is 32 mm. The frame structure is manufactured by the MakerBot Z18 3D printer using PLA material. For the scanning of the field, we used a 2-axis mobile platform to carry the microphone (Type 4935) for the point-by-point test. The measurement of the sound pressure is completed by the Lock-in system and software.

In the simulation and experiment setup, the lens is positioned along the X-axis; the middle point of the lens is same as the coordinate zero point. To measure the focal spot, the experimentally scanned region is from -0.2 m– 0.2 m along the X-axis and 0.3 m– 0.7 m along the Y-axis. The plane wave source of speaker array on the other side of X-axis is 70 mm away from the lens in a parallel position.

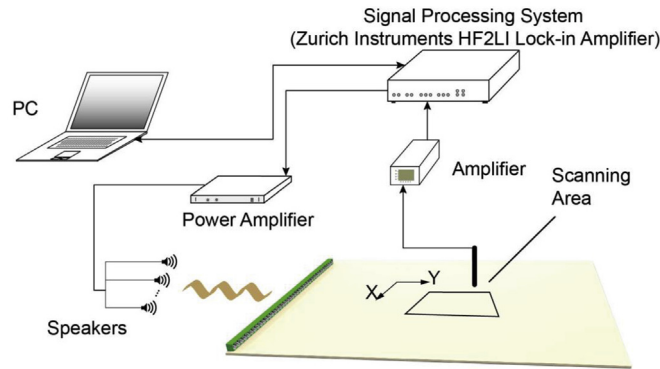


Fig. E.1. The sound field scanning setup. The Lock-in amplifier controlled by the computer works as both signal generation and data acquisition systems. An array of thirty speakers are in parallel to generate a plane wave positioned 0.07 m away from the metalens. For the scanning of the field, we measure the target region point by point with a step of 0.01 m.

Appendix F. A note for the working frequency range of the impedance tube

We just select 3 kHz–5 kHz in section 3.2, because of the performance of our lab made impedance tube. In low frequency, the tested parameter can be influenced by the thermal and viscous loss of the duct itself; in high frequency, which is higher than the cut frequency, the high-order mode can be generated to make the results lose the precision. When to demonstrate the difference between two cells, the error causes small influence on the outcome. However, when to discuss effective parameters in section 3.2, a more accurate data set is needed. Thus, the range 3 kHz–5 kHz can be accepted. The performance of the impedance tube can refer to Fig. F.1. We measured its transmission of sound pressure over the spectrum, due to the limited experimental conditions, in the low-frequency range (<3 kHz) it has a large attenuation while a slight fluctuation in the high-frequency range (>5 kHz).

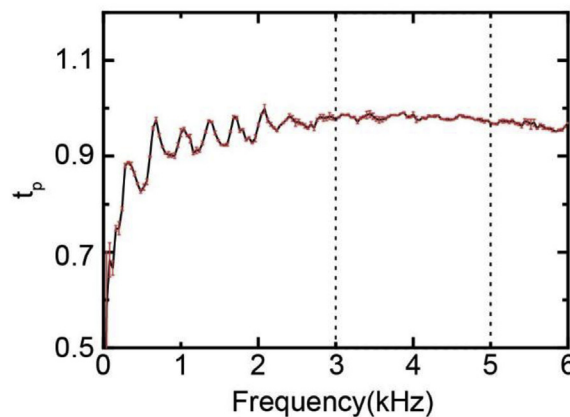


Fig. F.1. The measured energy transmission of the empty lab-made impedance tube.

Appendix G. Supplementary data

Supplementary data to this article can be found online at <https://doi.org/10.1016/j.jsv.2018.10.031>.

References

- [1] S. Qi, Y. Li, B. Assouar, Acoustic focusing and energy confinement based on multilateral metasurfaces, *Phys. Rev. Appl.* 7 (2017) 54006. <https://link.aps.org/doi/10.1103/PhysRevApplied.7.054006>.
- [2] Y. Li, B. Liang, X. Tao, X. Zhu, X. Zou, J. Cheng, Acoustic focusing by coiling up space, *Appl. Phys. Lett.* 101 (2012), 233508.
- [3] J. Zhao, B. Li, Z.N. Chen, C.-W. Qiu, Redirection of sound waves using acoustic metasurface, *Appl. Phys. Lett.* 103 (2013), 151604.
- [4] Y. Li, B. Liang, Z. Gu, X. Zou, J. Cheng, Reflected wavefront manipulation based on ultrathin planar acoustic metasurfaces, *Sci. Rep.* 3 (2013) 2546.
- [5] Y. Xie, W. Wang, H. Chen, A. Konneker, B.-I. Popa, S.A. Cummer, Wavefront Modulation and Subwavelength Diffractive Acoustics with an Acoustic Metasurface, 2014. *ArXiv Prepr. ArXiv1406.6306*.
- [6] G. Ma, M. Yang, S. Xiao, Z. Yang, P. Sheng, Acoustic metasurface with hybrid resonances, *Nat. Mater.* 13 (2014) 873.
- [7] Y. Li, B.M. Assouar, Acoustic metasurface-based perfect absorber with deep subwavelength thickness, *Appl. Phys. Lett.* 108 (2016) 63502.
- [8] S. Zhai, C. Ding, H. Chen, F. Shen, C. Luo, X. Zhao, Anomalous manipulation of acoustic wavefront with an ultrathin planar metasurface, *J. Vib. Acoust.* 138 (2016) 41019.

- [9] B. Yuan, Y. Cheng, X. Liu, Conversion of sound radiation pattern via gradient acoustic metasurface with space-coiling structure, *Appl. Phys. Express* 8 (2015) 27301.
- [10] W. Wang, Y. Xie, A. Konneker, B.-I. Popa, S.A. Cummer, Design and demonstration of broadband thin planar diffractive acoustic lenses, *Appl. Phys. Lett.* 105 (2014), 101904, <https://doi.org/10.1063/1.4895619>.
- [11] Y. Li, X. Jiang, R. Li, B. Liang, X. Zou, L. Yin, J. Cheng, Experimental realization of full control of reflected waves with subwavelength Acoustic metasurfaces, *Phys. Rev. Appl.* 2 (2014) 64002. <https://link.aps.org/doi/10.1103/PhysRevApplied.2.064002>.
- [12] J. Lan, Y. Li, Y. Xu, X. Liu, Manipulation of acoustic wavefront by gradient metasurface based on Helmholtz Resonators, *Sci. Rep.* 7 (2017) 10587.
- [13] Y. Li, X. Jiang, B. Liang, J. Cheng, L. Zhang, Metascreen-based acoustic passive phased array, *Phys. Rev. Appl.* 4 (2015) 24003. <https://link.aps.org/doi/10.1103/PhysRevApplied.4.024003>.
- [14] K. Tang, C. Qiu, M. Ke, J. Lu, Y. Ye, Z. Liu, Anomalous refraction of airborne sound through ultrathin metasurfaces, *Sci. Rep.* 4 (2014) 6517.
- [15] J. Mei, Y. Wu, Controllable transmission and total reflection through an impedance-matched acoustic metasurface, *New J. Phys.* 16 (2014) 123007.
- [16] C. Faure, O. Richoux, S. Félix, V. Pagneux, Experiments on metasurface carpet cloaking for audible acoustics, *Appl. Phys. Lett.* 108 (2016) 64103. <https://doi.org/10.1063/1.4941810>.
- [17] H. Esfahani, S. Karkar, H. Lissek, J.R. Mosig, Acoustic carpet cloak based on an ultrathin metasurface, *Phys. Rev. B* 94 (2016) 14302. <https://link.aps.org/doi/10.1103/PhysRevB.94.014302>.
- [18] C. Ding, H. Chen, S. Zhai, S. Liu, X. Zhao, The anomalous manipulation of acoustic waves based on planar metasurface with split hollow sphere, *J. Phys. D Appl. Phys.* 48 (2015) 45303.
- [19] Y.-F. Zhu, X.-Y. Zou, R.-Q. Li, X. Jiang, J. Tu, B. Liang, J.-C. Cheng, Dispersionless manipulation of reflected acoustic wavefront by subwavelength corrugated surface, *Sci. Rep.* 5 (2015).
- [20] Y.-F. Zhu, X.-D. Fan, B. Liang, J. Yang, J. Yang, L. Yin, J.-C. Cheng, Multi-frequency acoustic metasurface for extraordinary reflection and sound focusing, *AIP Adv.* 6 (2016), 121702, <https://doi.org/10.1063/1.4968607>.
- [21] X.-P. Wang, L.-L. Wan, T.-N. Chen, A.-L. Song, X.-W. Du, Broadband reflected wavefronts manipulation using structured phase gradient metasurfaces, *AIP Adv.* 6 (2016) 65320, <https://doi.org/10.1063/1.4954750>.
- [22] G.Y. Song, B. Huang, H.Y. Dong, Q. Cheng, T.J. Cui, Broadband focusing acoustic lens based on fractal metamaterials, *Sci. Rep.* 6 (2016).
- [23] Y. Tian, Q. Wei, Y. Cheng, Z. Xu, X. Liu, Broadband manipulation of acoustic wavefronts by pentamode metasurface, *Appl. Phys. Lett.* 107 (2015), 221906, <https://doi.org/10.1063/1.4936762>.
- [24] J. Lan, Y. Li, X. Liu, Broadband manipulation of refracted wavefronts by gradient acoustic metasurface with V-shape structure, *Appl. Phys. Lett.* 111 (2017), 263501, <https://doi.org/10.1063/1.5005950>.
- [25] L. Zigoneanu, B.-I. Popa, S.A. Cummer, Design and measurements of a broadband two-dimensional acoustic lens, *Phys. Rev. B* 84 (2011) 24305. <https://link.aps.org/doi/10.1103/PhysRevB.84.024305>.
- [26] G. Memoli, M. Caleap, M. Asakawa, D.R. Sahoo, B.W. Drinkwater, S. Subramanian, Metamaterial bricks and quantization of meta-surfaces, *Nat. Commun.* 8 (2017) 14608, <https://doi.org/10.1038/ncomms14608>.
- [27] K. Li, B. Liang, J. Yang, J. Yang, J. Cheng, Acoustic broadband metacouplers, *Appl. Phys. Lett.* 110 (2017), 203504, <https://doi.org/10.1063/1.4983674>.
- [28] X. Zhu, K. Li, P. Zhang, J. Zhu, J. Zhang, C. Tian, S. Liu, Implementation of Dispersion-free Slow Acoustic Wave Propagation and Phase Engineering with Helical-structured Metamaterials, vol. 7, 2016, p. 11731.
- [29] Y. Ding, E.C. Statharas, K. Yao, M. Hong, A broadband acoustic metamaterial with impedance matching layer of gradient index, *Appl. Phys. Lett.* 110 (2017) 241903, <https://doi.org/10.1063/1.4986472>.
- [30] L. Kun, L. Bin, Y. Jing, Y. Jun, C. Jian-chun, Broadband transmission-type coding metamaterial for wavefront manipulation for airborne sound, *Appl. Phys. Express* 11 (2018) 77301. <http://stacks.iop.org/1882-0786/11/i=7/a=077301>.
- [31] H. Esfahani, H. Lissek, J.R. Mosig, Generation of acoustic helical wavefronts using metasurfaces, *Phys. Rev. B* 95 (2017) 24312. <https://link.aps.org/doi/10.1103/PhysRevB.95.024312>.
- [32] V. Fokin, M. Ambati, C. Sun, X. Zhang, Method for retrieving effective properties of locally resonant acoustic metamaterials, *Phys. Rev. B* 76 (2007), 144302.
- [33] H.P. Helfrich, D. Zwick, A trust region algorithm for parametric curve and surface fitting, *J. Comput. Appl. Math.* 73 (1996) [119]–[134]. [https://doi.org/10.1016/0377-0427\(96\)00039-8](https://doi.org/10.1016/0377-0427(96)00039-8).
- [34] D.R. Raichel, *The Science and Applications of Acoustics*, Springer Science & Business Media, 2006.
- [35] Z. Li, D.-Q. Yang, S.-L. Liu, S.-Y. Yu, M.-H. Lu, J. Zhu, S.-T. Zhang, M.-W. Zhu, X.-S. Guo, H.-D. Wu, Broadband gradient impedance matching using an acoustic metamaterial for ultrasonic transducers, *Sci. Rep.* 7 (2017) 42863.
- [36] M. Abramowitz, I.A. Stegun, *Handbook of Mathematical Functions: with Formulas, Graphs, and Mathematical Tables*, Courier Corporation, 1965.